PAPER

Topological phonons and electronic structure of Li_2BaSi class of semimetals

IOP Publishing Journal of Physics: Condensed Matter
J. Phys.: Condens. Matter **34** (2022) 125502 (8pp) https://doi.org/10.1088/1361-648X/ac4441

Topological phonons and electronic structure of Li_2BaSi class of semimetals

Vineet Kumar Sharma[1], Birender Singh[2], Anan Bari Sarkar[3], Mayanak K Gupta[4,5], Ranjan Mittal[4,5], Amit Agarwal[3], Bahadur Singh[2,*] and V Kanchana[1,*]

[1] Department of Physics, Indian Institute of Technology Hyderabad, Kandi 502285, Sangareddy, Telangana, India
[2] Department of Condensed Matter Physics and Materials Science, Tata Institute of Fundamental Research, Mumbai 400005, India
[3] Department of Physics, Indian Institute of Technology, Kanpur 208016, India
[4] Solid State Physics Division, Bhabha Atomic Research Centre Trombay, Mumbai 400085, India
[5] Homi Bhabha National Institute, Anushaktinagar, Mumbai 400094, India

E-mail: bahadur.singh@tifr.res.in and kanchana@iith.ac.in

Received 12 August 2021, revised 5 December 2021
Accepted for publication 17 December 2021
Published 6 January 2022

Abstract

Extension of the topological concepts to the bosonic systems has led to the prediction of topological phonons in materials. Here we discuss the topological phonons and electronic structure of Li_2BaX (X = Si, Ge, Sn, and Pb) materials using first-principles theoretical modelling. A careful analysis of the phonon spectrum of Li_2BaX reveals an optical mode inversion with the formation of nodal line states in the Brillouin zone. Our electronic structure results reveal a double band inversion at the Γ point with the formation of inner nodal-chain states in the absence of spin–orbit coupling (SOC). Inclusion of the SOC opens a materials-dependent gap at the band crossing points and transitions the system into a trivial insulator state. We also discuss the lattice thermal conductivity and transport properties of Li_2BaX materials. Our results show that coexisting phonon and electron nontrivial topology with robust transport properties would make Li_2BaX materials appealing for device applications.

Keywords: topological phonons, topological nodal chain states, thermal conductivity, transport properties

(Some figures may appear in colour only in the online journal)

1. Introduction

The classification of topological quantum states beyond insulators has led to the prediction of topological semimetals (TSMs) with protected bulk and surface states [1–3]. Widely investigated TSMs include Dirac semimetals (DSMs) in which the doubly-degenerate bands cross at the high-symmetry points or lines in the bulk Brillouin zone (BZ) in presence of time-reversal (𝕋), inversion (𝕀), and crystalline symmetries [2, 3]. Breaking either of 𝕋 or 𝕀 leads to the formation of Weyl fermion states in materials [4]. Other TSMs include nodal-line semimetals (NLSMs) in which the crossings bands form closed loops or lines in the BZ [5–7]. Based on the underlying crystal symmetries, the nodal lines in NLSMs can form interesting nodal structures such as nodal chain, Hopf-link, starfruit-like nodal lines [8, 9], among others with their unique physical properties. TSMs have been realized in experiments by observing Dirac fermions states in Na_3Bi and Cd_3As_2 [2, 10], Weyl fermion states in TaAs [11, 12], LaAlGe [13], $MoTe_2$ materials [14], and nodal-line states in ZrSiS [15], $PbTaSe_2$ [16], Co_2MnGa [17] through transport and spectroscopy measurements.

* Authors to whom any correspondence should be addressed.

Table 1. Optimized lattice parameters of Li_2BaX and associated experimental parameters [51].

	Experiment			GGA			LDA		
Compound	*a* (Å)	*b* (Å)	*c* (Å)	*a* (Å)	*b* (Å)	*c* (Å)	*a* (Å)	*b* (Å)	*c* (Å)
Li_2BaSi	6.74	4.68	6.26	6.69	4.66	6.38	6.53	4.56	6.22
Li_2BaGe	6.76	4.71	6.30	6.73	4.71	6.44	6.54	4.59	6.26
Li_2BaSn	7.20	4.92	6.33	7.19	4.94	6.49	7.04	4.81	6.24
Li_2BaPb	7.16	4.96	6.45	7.25	5.02	6.60	7.07	4.87	6.31

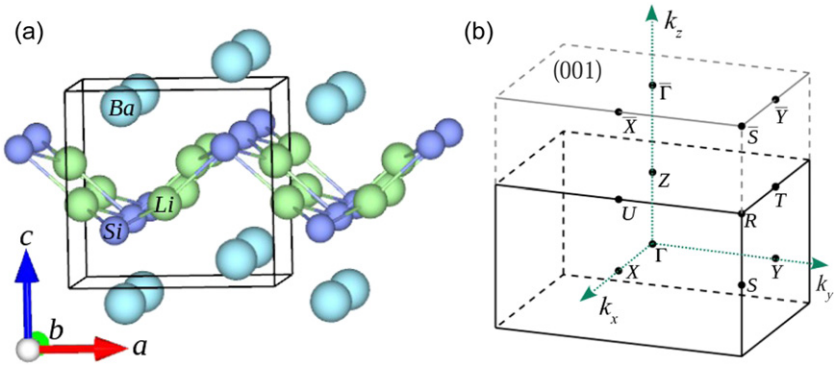

Figure 1. (a) Crystal structure of Li_2BaSi. Green, blue, and cyan spheres identify Li, Si, and Ba atoms, respectively. (b) Bulk BZ and projected (001) surface BZ. The relevant high-symmetry points are marked.

The topological concepts of electronic states have been generalized to phonons that result in the prediction of topological phonons in various materials. The phonons play an essential role in materials properties including thermal conductivity, thermoelectricity, superconductivity, or specific heat. Identifying materials with topological phononic states would not only enrich our understanding of topological concepts in bosonic systems but also provides a crucial paradigm for investigating bosonic quasiparticles in materials. By considering the phonons and crystal symmetries, various topological phonons states such as doubly-generate phonons in transition-metal monosilicides [18], triply-degenerate phonons in TiS, ZrSe, and HfTe [19, 20], and nodal-line phonons in graphene have been predicted [19].

TSMs are attractive since they realize exotic states and properties interesting for quantum information and spintronic applications [21–26]. They also support diverse electromagnetic responses such as loop Hall effects [27, 28], unconventional optical response [29, 30], and high-temperature superconductivity [31–33]. Motivated by these exotic properties, we explore the topological electron and phonon structure of recently introduced Li-based TSMs with inner-nodal chain states in Li_2BaX (M = Si, Ge, Sn, and Pb) [34–36]. Our systematic first-principles calculations reveal that Li_2BaX materials support interesting nodal-chain phonons with topological states in the optical branches of the phonon spectrum. The electronic spectrum supports inner-nodal chain states without spin–orbit coupling (SOC). A material-dependent hybridization gap opens up at the crossing point with the inclusion of SOC that drives the systems into a trivial topological state. We also investigate lattice thermal conductivity and transport properties of Li_2BaX materials. Our results show that Li_2BaX offers a good platform to investigate topological electron and phonon states in materials.

2. Methodology and crystal structure

First-principles calculations were performed with the projector augmented wave method as implemented in the Vienna *ab initio* simulation package [37, 38]. The exchange–correlation effects were considered using both the generalized gradient approximation (GGA) [39] and local density approximation (LDA) [40]. We found lattice parameters obtained with the GGA were in better accord with the experiments (table 1), which are ultimately used to calculate our results. An energy cutoff of 900 eV was used for the plane wave basis and an $8 \times 8 \times 8$ Γ centered *k*-mesh was used for BZ sampling. The energy and force convergence tolerance were set as 10^{-8} eV and 10^{-2} eV $Å^{-1}$, respectively. The first-principles tight-binding Hamiltonians [41, 42] were generated for both the electron and phonon system to compute the topological properties using the WannierTools package [43, 44]. The phonon dispersion curves were obtained with the frozen phonon method using the phonopy [45]. Higher-order force constants were obtained within the supercell approach by applying a finite displacement of atoms of 0.03 Å, which were subsequently used to calculate the lattice thermal conductivity κ_l with the phono3py [46]. We calculated transport properties within the constant scattering time approximation and rigid-band approximation using the BoltzTraP code [47–50].

Li_2BaX belongs to orthorhombic crystal lattice with nonsymmorphic space group *Pmmn* (No. 59) [51]. The crystal

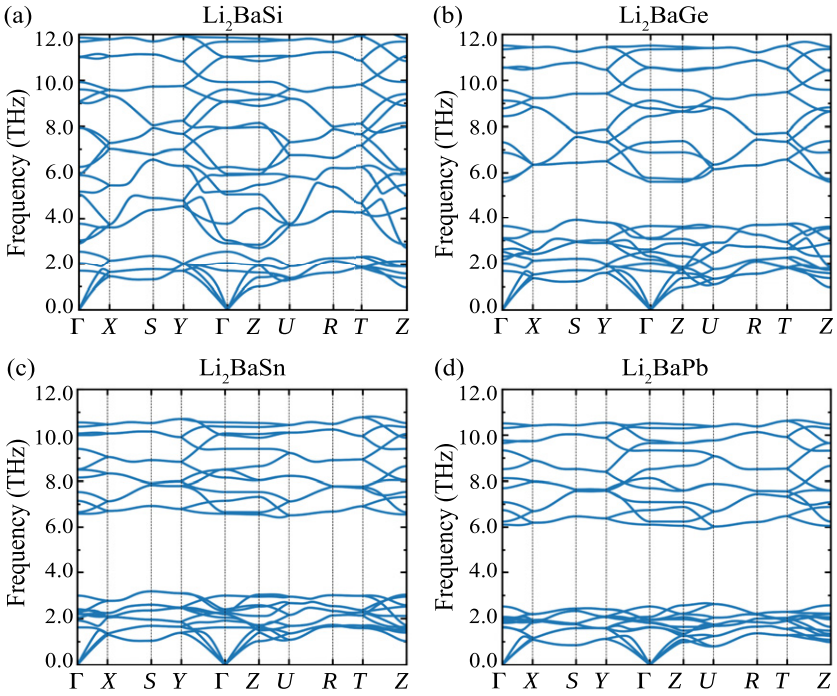

Figure 2. Calculated phonon dispersion of (a) Li_2BaSi, (b) Li_2BaGe, (c) Li_2BaSn, and (d) Li_2BaPb. Various optical phonon branches cross to generate an inverted region in the optical spectrum.

structure with taking Li_2BaSi as an explicit example is shown in figure 1(a). It consists of a buckled network of Li and Si atoms whereas Ba atoms follow these networks to generate an orthorhombic structure. The important symmetries of the crystal structure include an inversion $\mathbb{I}$, mirror planes M_x and M_y, and glide mirror plane $\tilde{M}_z = \{M_z|\frac{1}{2},\frac{1}{2},0\}$ symmetries. Additionally, the system respects time-reversal symmetry $\mathbb{T}$. The bulk and (001) plane projected surface BZs are shown in figure 1(b).

3. Results and discussion

3.1. Topological phonons in Li_2BaX

We present the calculated phonon spectrum of Li_2BaX materials in figure 2. The lack of the imaginary phonon frequency in the full BZ ensures the dynamical stability of Li_2BaX. There is an interaction between the acoustic phonon branches and the low-lying optical phonon bands. A narrow phonon gap is seen between the low-frequency and high-frequency optical phonon modes of Li_2BaSi (figure 2(a)). These phonon–phonon interactions and phonon-gap enhance as one moves from Li_2BaSi to Li_2BaPb compound (figure 2(d)). To further explore the dominant atomic contributions to the phonon bands, we compute the projected phonon density of states (not shown for brevity). We find that Ba atoms contribute the low-lying phonons up to ∼3 THz frequency, Si atoms dominate between 3–7 THz frequency, and the Li atoms give rise to the high-frequency phonon modes (figure 2(a)). Replacing Si in Li_2BaX with heavier Ge, Sn, or Pb atoms pushes the X atomic phonons to the low-frequency region, thereby enhancing the acoustic and low-lying optical phonon interactions and phonon bandgap in the optical phonon regime. This enhancement in phonon–phonon interaction may lead to low thermal conductivity as discussed below.

To elucidate the underlying topological phononic states in Li_2BaX, we constructed material-specific phonon tight-binding Hamiltonian for Li_2BaSi as a representative case. Figure 3(a) shows the optical phonon bands between 6 to 8 THz. Various band crossings are seen at the high-symmetry directions between B_{2u} and B_{2g} symmetry states. A careful exploration of these band crossings in the bulk BZ shows that they form three distinct nodal lines in a cylinder-like nodal arrangement. The two closed loops lie on the $k_z = 0$ and $k_z = \pi$ planes whereas the open lines form on the $k_x = 0$ plane (figures 3(b) and (c)). Our symmetry analysis shows that B_{2u} and B_{2g} states carry opposite M_x and M_z mirror eigenvalues. The nodal crossings are thus protected against band hybridizations. The topological protection of these nodal line states is further confirmed by calculating the nonzero Berry phase along a $k-$space loop inclosing the nodal lines. Figures 3(d) and (e) show the projected bulk phonon and surface band structure of (001) surface. The projected nodal line states and associated topological states are evident along the high-symmetry directions. We find that the topological states are mostly masked by the bulk projection except along the $\overline{X}$–$\overline{S}$ direction which is shown in the inset of figure 3(e).[6] The constant frequency contour at 7.15 THz is shown in figure 3(f).

[6] Note that the non-trivial phonon surface states are associated with specific lattice vibrations. Such states can provide highly directional non-dissipative energy propagation with applications in thermal transport, low-dissipation transmission, and phonon waveguides.

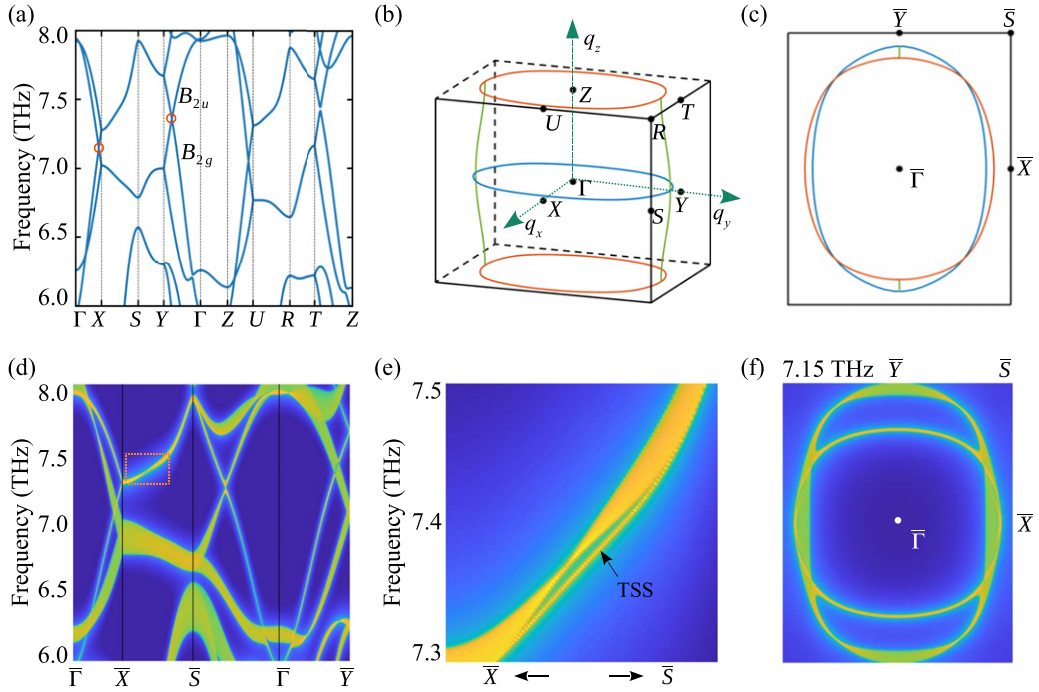

Figure 3. (a) Selected region of the optical phonon spectrum of Li_2BaSi (figure 2(a)). The bulk nodal crossings between B_{2u} and B_{2g} states are seen along the Γ–X, Γ–Y, Z–U, and T–Z directions. (b) Illustration of the calculated nodal crossings in the full bulk BZ. (c) (001) plane projected nodal lines. (d) Surface phonon spectrum in 001 plane. (e) The topological surface states for selected frequency window in surface phonon spectrum. (f) Constant frequency contours calculated at 7.15 THz.

3.2. *Topological electronic structure of* Li_2BaX

We present the calculated bulk band structure of Li_2BaSi without SOC in figure 4(a). The presence of both the hole and electron bands at the Fermi level reveals the semimetal state of Li_2BaSi. Interestingly, the electron bands with $\Gamma^{2-}(B_{3u})$ symmetry are seen to cross with $\Gamma^{+}(A_{1g})$ hole bands along the Γ–X, Γ–Y, and Γ–Z directions. A full BZ exploration of these crossing points reveal that they form nodal lines on the $k_z = 0$ and $k_y = 0$ plane (figures 4(e)–(g)). These nodal lines cross along at the $k_x = 0$ plane thereby forming an inner nodal chain structure. Figure 4(b) shows the calculated (010) surface energy dispersion of Li_2BaSi. The projected bulk nodal lines are seen along the $\overline{\Gamma}$–$\overline{X}$ and $\overline{\Gamma}$–$\overline{Z}$ directions. The associated drumhead surface states (DSSs) are resolved which are indicated with a black arrow in figure 4(b). The bulk and surface band structure of Li_2BaSi with the inclusion of SOC is shown in figures 4(c) and (d), respectively. The bulk nodal crossings in presence of SOC are gapped, generating a continuous local bandgap between valence and conduction bands at each k point. Our Z_2 invariants calculations reveal a trivial nature with $(\nu_0, \nu_1\nu_2\nu_3) = (0, 000)$. This is consistent with the surface states calculations which show gapped DSSs without the formation of Dirac-like states within the bulk bandgap. These results reveal that Li_2BaSi realizes an SOC-driven crossover from an inner-nodal chain semimetal to a trivial band insulator.

We present calculated bulk and surface electronic dispersion of Li_2BaPb in figure 5. This system realizes an inner-nodal chain structure without SOC and a trivial insulator state with SOC similar to Li_2BaSi. However, the valence and conduction band overlap, and the size of the gap opening at the band crossing points are enlarged. This behavior is consistent with the large SOC strength of Pb atoms as compared to the Si atoms. Our results of Li_2BaX materials thus reveal that while their topological nature remains robust with a change in X atom, the band overlap and gap opening at the crossing points are sensitive to the X atom in Li_2BaX.

3.3. *Transport analysis*

Having discussed the topological electron and phonon spectrum, we now discuss the thermal and electrical transport of Li_2BaX. It is known that the highly interacting phonon modes result in low lattice thermal conductivity. Since phonon–phonon interaction is higher in Li_2BaPb, it would have lower thermal conductivity. To illustrate this scenario, we calculate the lattice thermal conductivity of Li_2BaX using the phono3py module of phonopy code. We consider a large $3 \times 4 \times 3$ supercell with an atomic displacement of 0.03 Å to obtain force constants. The calculated thermal conductivity (κ_l) of Li_2BaSi along three crystallographic directions is shown in figure 6. The thermal conductivity κ_l is anisotropic due to the orthorhombic symmetry of the associated crystal structure. κ_l decreases with an increase in the temperature. Figure 6(b) shows the calculated phonon lifetime at 300 K, where the black dots display phonon distribution at a frequency and the density of phonon modes is displayed in a color scale. We clearly see a gap in the phonon lifetime for the 2–4.5 THz frequency range which is consistent with the calculated phonon curves. There are few regions without phonon modes but have finite colors which show the least phonon density regions. We observe a shorter phonon lifetime for the

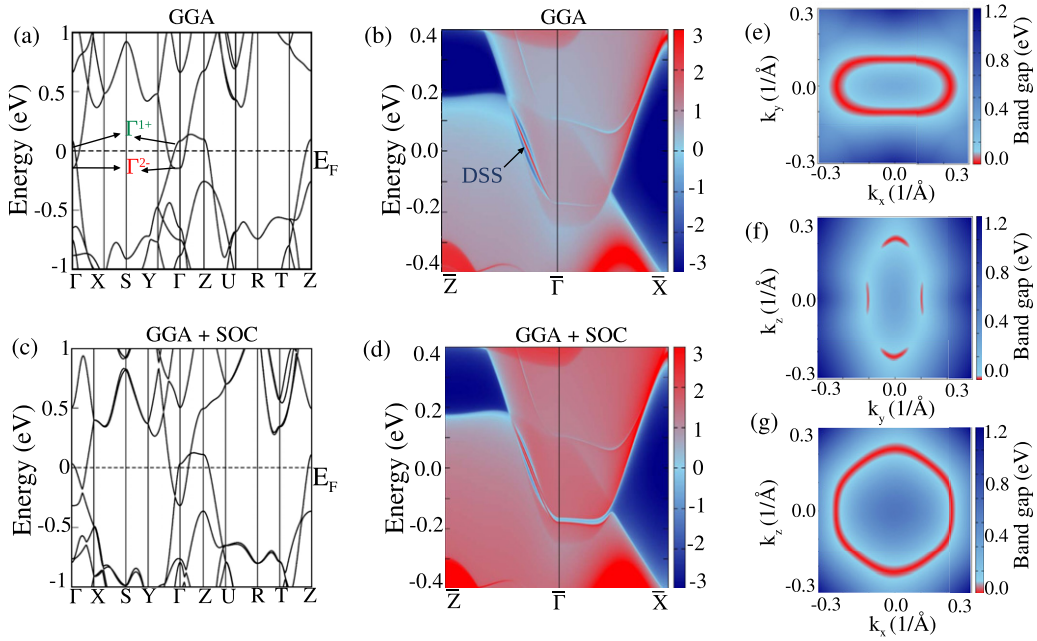

Figure 4. (a) Calculated bulk band structure of Li_2BaSi without SOC. (b) The surface band structure of (010) surface of Li_2BaSi without SOC. The DSSs are marked with the black arrow. Colorbar shows the surface states weights. (c) and (d) Same as (a) and (b) but with the inclusion of SOC. The calculated energy gap between valence and conduction bands on (e) $k_z = 0$, (f) $k_x = 0$, and (g) $k_y = 0$ planes without SOC. The red color identifies the zero energy gap region on various planes.

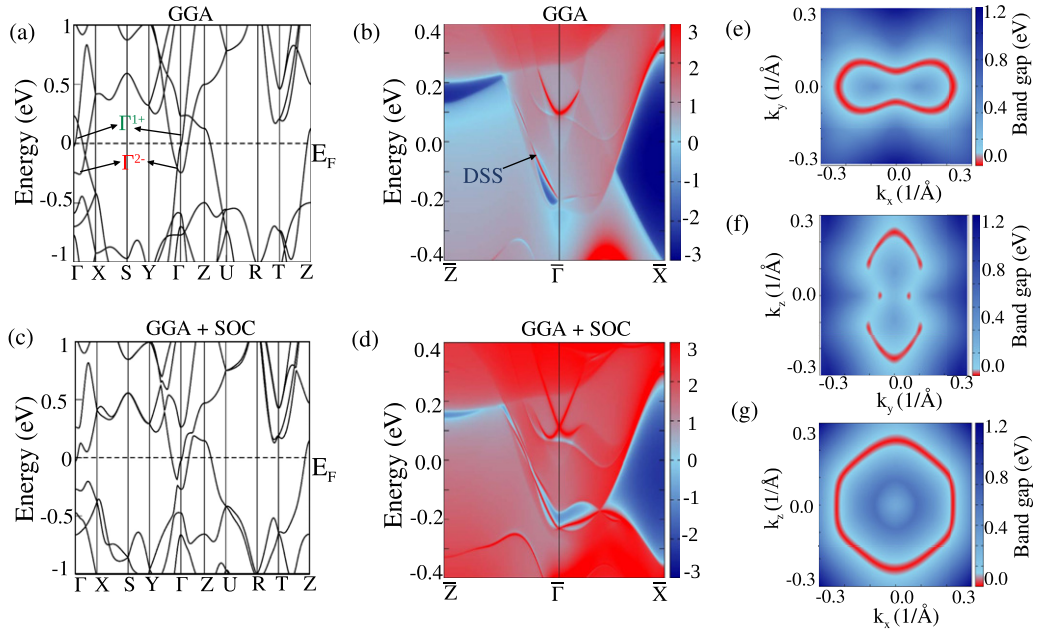

Figure 5. (a) Calculated bulk band structure of Li_2BaPb without SOC. (b) The surface band structure of (010) surface of Li_2BaPb without SOC. The DSSs are marked with the black arrow. (c) and (d) Same as (a) and (b) but with the inclusion of SOC. The calculated energy gap between valence and conduction bands on (e) $k_z = 0$, (f) $k_x = 0$, and (g) $k_y = 0$ planes without SOC. The red color identifies the zero energy gap region on various planes.

high-frequency region than the low-frequency region due to enhanced phonon–phonon interaction. This may lead to a low lattice thermal conductivity at high temperature and reflect the effects of nontrivial phonon structure [52].

Figure 6(c) shows accumulative lattice thermal conductivity as a function of the mean free path for Li_2BaSi. The phonon mean free path should be comparable to the grain size of the materials to enhance properties such as thermoelectric properties through structural engineering [53]. The accumulative lattice thermal conductivity increases monotonically with an increase in the mean free path and saturates near 400 nm. Figure 7 shows the calculated thermal conductivity, phonon

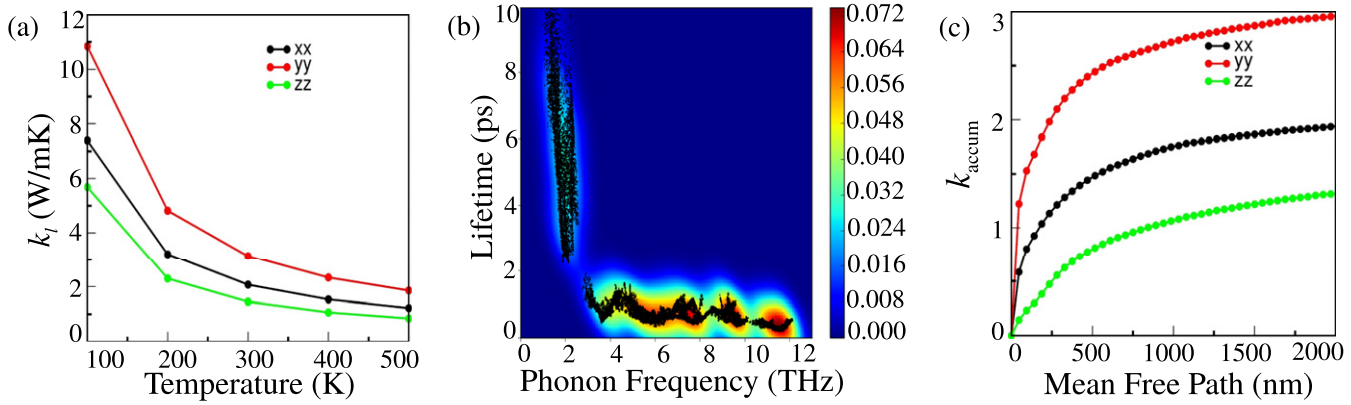

Figure 6. (a) Calculated lattice thermal conductivity of Li_2BaSi as a function of temperature. (b) Phonon lifetime as a function of phonon frequency. The black dots show the phonon distribution at a particular frequency. The color bar represents the density of phonon modes where the maximum and minimum values of the phonon density are shown with red and blue, respectively. (c) Accumulative lattice thermal conductivity as a function of the mean free path. It saturates for a larger mean free path.

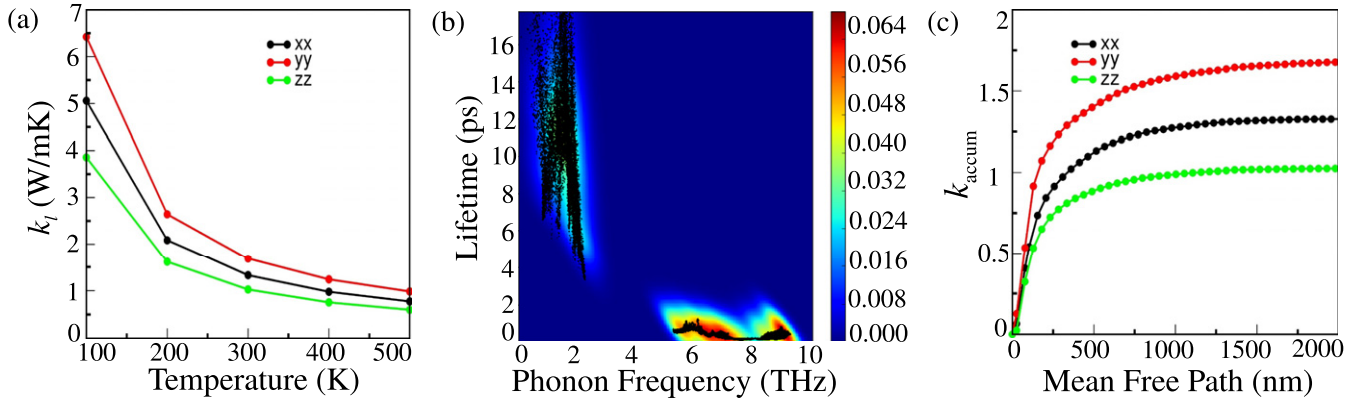

Figure 7. (a) Calculated lattice thermal conductivity of Li_2BaPb as a function of temperature. (b) Phonon lifetime as a function of phonon frequency. The black dots show the phonon distribution at a particular frequency. The color bar represents the density of phonon modes where the maximum and minimum values of the phonon density are shown with red and blue, respectively. (c) Accumulative lattice thermal conductivity as a function of the mean free path. It saturates for a larger mean free path.

lifetimes, and accumulative lattice thermal conductivity for Li_2BaPb. Its thermal conductivity is lower than Li_2BaSi as expected from the heavier size of the Pb atoms. Other properties remain robust for these materials. Moreover, the calculated thermal conductivity in these materials is found to be low than other reported topological materials [54, 55]. These results indicate that Li_2BaX materials would be favorable for structural engineering.

The low lattice thermal conductivity and nontrivial properties of Li_2BaX motivates us further to investigate the electronic transport of these materials, which is useful for device applications [56–59]. We calculate carrier mobility within the relaxation time approximation using Boltzmann transport theory. The carrier concentration and carrier mobilities as a function of temperature are shown in figure 8 for Li_2BaSi. It is seen that the calculated electron and hole concentrations stay close in numbers in the low temperature range, ensuring the robust semi-metallic nature of Li_2BaSi. Interestingly, the electron and hole carriers are nearly equal at a temperature of 140 K. This infers that this material possess charge compensation that may lead to a large magnetoresistance. The calculated directional dependent mobility as a function of temperature for the electron and hole carriers concentrations of 1×10^{20} cm^{-3} is shown in figure 8(b). Both the electron and hole mobilities remain the same. Notably, the calculated value of hole mobilities at temperature $\sim$ 140 K are 1.48×10^{16} cm^2 V^{-1} s^{-2}, 3.25×10^{16} cm^2 V^{-1} s^{-2} and 1.51×10^{16} cm^2 V^{-1} s^{-2} along a, b, and c axes, respectively. The electron mobilities are 1.34×10^{16} cm^2 V^{-1} s^{-2}, 3.09×10^{16} cm^2 V^{-1} s^{-2} and 1.75×10^{16} cm^2 V^{-1} s^{-2} along the three crystallographic axes. These values of electron mobilities, as well as the estimated scattering time which is of the order of 10^{-12} to 10^{-13} s, are comparable to ZrSiSe class of nodal-line semimetals [60, 61] and various other DSMs and WSMs [62–64]. Notably, we calculate transport properties within a semi-classical approach under relaxation time approximation which may not fully account for the effects of quantum geometry and topological states.

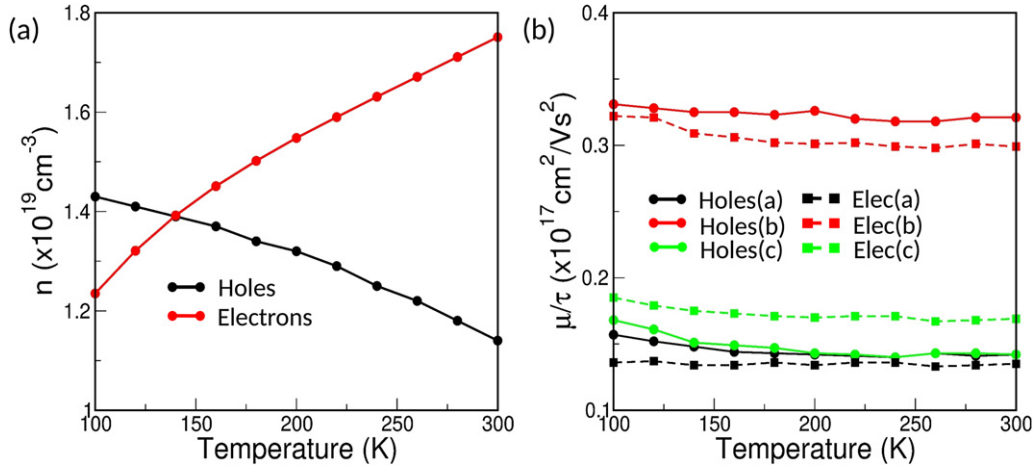

Figure 8. (a) The carrier concentration as a function of temperature and (b) the mobility as a function of temperature for Li_2BaSi.

4. Conclusion

We present the topological phonon and electronic structure of Li_2BaX semimetals based on the first-principles theoretical modeling. The calculated phonon spectrum lacks imaginary phonon frequencies, which shows the dynamical stability of Li_2BaX materials. Interestingly, we observe band inversion in the optical phonon bands. These bands cross to form a nontrivial bulk nodal-line structure with associated nontrivial surface states. The electronic properties reveal a semi-metallic nature of the band structure with the presence of both the electron and hole bands at the Fermi level. It is found that both the electron and hole bands cross in the bulk BZ and form an inner-nodal chain structure without SOC. In presence of SOC, a material-dependent band gap generates at the nodal crossings and the system transitions to a trivial insulator state. We have also calculated the thermal and electrical transport of Li_2BaX materials to showcase the effect of observed phonon and electronic structure. The lattice thermal conductivity is found to be low in comparison to the other known semimetals. We have seen nearly equal electron and hole concentrations which signals that these materials may show large magnetoresistance. Our results indicate that Li_2BaX materials offer a good platform to explore topological phonon and electronic states with robust transport properties.

Acknowledgments

VKS and VK acknowledge IIT Hyderabad for providing computational facilities and BRNS Project with Sanction No. 58/14/13/2019-BRNS for financial support. VKS acknowledges MoE for research fellowship. The work at TIFR Mumbai is supported by the Department of Atomic Energy of the Government of India under Project Number 12-R & D-TFR-5.10-0100. ABS and AG acknowledge IIT Kanpur, Science Engineering and Research Board (SERB), and the Department of Science and Technology (DST) India, for financial support.

Data availability statement

The data generated and/or analysed during the current study are not publicly available for legal/ethical reasons but are available from the corresponding author on reasonable request.

ORCID iDs

Mayanak K Gupta https://orcid.org/0000-0002-9016-2438
Ranjan Mittal https://orcid.org/0000-0003-3729-9352
Amit Agarwal https://orcid.org/0000-0001-6399-7264
Bahadur Singh https://orcid.org/0000-0002-2013-1126
V Kanchana https://orcid.org/0000-0003-1575-9936

References

[1] Bansil A, Lin H and Das T 2016 *Rev. Mod. Phys.* **88** 021004
[2] Wang Z, Sun Y, Chen X-Q, Franchini C, Xu G, Weng H, Dai X and Fang Z 2012 *Phys. Rev.* B **85** 195320
[3] Murakami S 2007 *New J. Phys.* **9** 356
[4] Zyuzin A A, Wu S and Burkov A A 2012 *Phys. Rev.* B **85** 165110
[5] Yan Z, Bi R, Shen H, Lu L, Zhang S C and Wang Z 2017 *Phys. Rev.* B **96** 041103
[6] Bi R, Yan Z, Lu L and Wang Z 2017 *Phys. Rev.* B **96** 201305
[7] Bzdušek T, Wu Q, Rüegg A, Sigrist M and Soluyanov A A 2016 *Nature* **538** 75–8
[8] Chang G *et al* 2017 *Phys. Rev. Lett.* **119** 156401
[9] Singh B, Mardanya S, Su C, Lin H, Agarwal A and Bansil A 2018 *Phys. Rev.* B **98** 085122
[10] Wang Z, Weng H, Wu Q, Dai X and Fang Z 2013 *Phys. Rev.* B **88** 125427
[11] Lv B Q *et al* 2015 *Phys. Rev.* X **5** 031013
[12] Huang S-M *et al* 2015 *Nat. Commun.* **6** 7373
[13] Xu S Y *et al* 2017 *Sci. Adv.* **3** e1603266
[14] Wang Z, Gresch D, Soluyanov A A, Xie W, Kushwaha S, Dai X, Troyer M, Cava R J and Bernevig B A 2016 *Phys. Rev. Lett.* **117** 056805
[15] Fu B B *et al* 2019 *Sci. Adv.* **5** eaau6459
[16] Bian G *et al* 2016 *Nat. Commun.* **7** 10556

[17] Belopolski I *et al* 2019 *Science* **365** 1278–81
[18] Zhang T, Song Z, Alexandradinata A, Weng H, Fang C, Lu L and Fang Z 2018 *Phys. Rev. Lett.* **120** 016401
[19] Li J, Xie Q, Ullah S, Li R, Ma H, Li D, Li Y and Chen X Q 2018 *Phys. Rev.* B **97** 054305
[20] Xie Q, Li J, Ullah S, Li R, Wang L, Li D, Li Y, Yunoki S and Chen X-Q 2019 *Phys. Rev.* B **99** 174306
[21] Koshino M and Ando T 2010 *Phys. Rev.* B **81** 195431
[22] Zyuzin A A and Burkov A A 2012 *Phys. Rev.* B **86** 115133
[23] Hosur P and Qi X 2013 *C. R. Phys.* **14** 857–70
[24] Fukushima K, Kharzeev D E and Warringa H J 2008 *Phys. Rev.* D **78** 074033
[25] Guin S N *et al* 2021 *Adv. Mater.* **33** 2006301
[26] Yang S A 2016 *SPIN* **06** 1640003
[27] Yang H-Y *et al* 2020 *APL Mater.* **8** 011111
[28] Yang H-Y *et al* 2021 *Phys. Rev.* B **103** 115143
[29] Liu Y, Yu Z-M and Yang S A 2017 *Phys. Rev.* B **96** 121101
[30] Chang G *et al* 2017 *Phys. Rev. Lett.* **119** 206401
[31] Pang G M *et al* 2016 *Phys. Rev.* B **93** 060506
[32] Wang L S, Fang Y Q, Huang Y Y, Cheng E J, Ni J M, Pan B L, Xu Y, Huang F Q and Li S Y 2020 *Phys. Rev.* B **102** 024523
[33] Shimamura N *et al* 2018 *ACS Nano* **12** 10977–83
[34] Zhang X, Jin L, Dai X, Chen G and Liu G 2018 *J. Phys. Chem. Lett.* **9** 5358–63
[35] Axel H, Müller W, Schäfer H and Weiss A 1967 *Z. Naturforsch.* B **22** 1081
[36] Wang X, Ding G, Cheng Z, Wang X-L, Zhang G and Yang T 2020 *J. Mater. Chem.* C **8** 5461–6
[37] Kresse G and Furthmüller J 1996 *Comput. Mater. Sci.* **6** 15–50
[38] Kresse G and Joubert D 1999 *Phys. Rev.* B **59** 1758–75
[39] Perdew J P, Burke K and Ernzerhof M 1996 *Phys. Rev. Lett.* **77** 3865–8
[40] Calais J-L 1993 *Int. J. Quantum Chem.* **47** 101
[41] Marzari N and Vanderbilt D 1997 *Phys. Rev.* B **56** 12847–65
[42] Mostofi A A, Yates J R, Lee Y-S, Souza I, Vanderbilt D and Marzari N 2008 *Comput. Phys. Commun.* **178** 685–99
[43] Wu Q, Zhang S, Song H-F, Troyer M and Soluyanov A A 2018 *Comput. Phys. Commun.* **224** 405–16
[44] Sancho M P L, Sancho J M L, Sancho J M L and Rubio J 1985 *J. Phys. F: Met. Phys.* **15** 851–8
[45] Togo A, Oba F and Tanaka I 2008 *Phys. Rev.* B **78** 134106
[46] Togo A, Chaput L and Tanaka I 2015 *Phys. Rev.* B **91** 094306
[47] Madsen G K H and Singh D J 2006 *Comput. Phys. Commun.* **175** 67–71
[48] Scheidemantel T J, Ambrosch-Draxl C, Thonhauser T, Badding J V and Sofo J O 2003 *Phys. Rev.* B **68** 125210
[49] Jodin L, Tobola J, Pecheur P, Scherrer H and Kaprzyk S 2004 *Phys. Rev.* B **70** 184207
[50] Chaput L, Pécheur P, Tobola J and Scherrer H 2005 *Phys. Rev.* B **72** 085126
[51] Stoiber D, Bobnar M, Höhn P and Niewa R 2017 *Z. Naturforsch.* B **72** 847–53
[52] Guo R, Wang X, Kuang Y and Huang B 2015 *Phys. Rev.* B **92** 115202
[53] Wang C, Chen Y B, Yao S H and Zhou J 2019 *Phys. Rev.* B **99** 024310
[54] Kaur K, Dhiman S and Kumar R 2017 *Phys. Lett.* A **381** 339–43
[55] Guo S-D, Wang Y-H and Lu W-L 2017 *New J. Phys.* **19** 113044
[56] Sasmal S, Mondal R, Kulkarni R, Thamizhavel A and Singh B 2020 *J. Phys.: Condens. Matter* **32** 335701
[57] Takatsu H, Ishikawa J J, Yonezawa S, Yoshino H, Shishiduo T, Oguchi T, Murata K and Maeno Y 2013 *Phys. Rev. Lett.* **111** 056601
[58] Mun E, Ko H, Miller G J, Samolyuk G D, Budko S L and Canfield P C 2012 *Phys. Rev.* B **85** 035135
[59] Wang K, Graf D, Li L, Wang L and Petrovic C 2014 Anisotropic giant magnetoresistance in $NbSb_2$ *Sci. Rep.* **4** 7328
[60] Guo L *et al* 2019 *ACS Appl. Electron. Mater.* **1** 869–876
[61] Hu J *et al* 2016 *Phys. Rev. Lett.* **117** 016602
[62] Liu C, Hellerstedt J, Edmonds M T and Fuhrer M S 2017 *Phys. Rev.* B **96** 235412
[63] Zheng G *et al* 2016 *Phys. Rev.* B **93** 115414
[64] Neupane M *et al* 2014 *Nat. Commun.* **5** 3786